3D printing of porcelain: finite element simulation of anisotropic sintering

Charles Manière, Christelle Harnois, Sylvain Marinel

3D printing of porcelain: finite element simulation of anisotropic sintering

Charles Manière[1]*, Christelle Harnois[1], Sylvain Marinel[1]

1. Normandie Univ, ENSICAEN, UNICAEN, CNRS, CRISMAT, 14000, Caen, France

Keywords
3D printing; Finite Element Simulation; Anisotropy; Mesoscale Simulation; Sintering

Abstract

Sintering is a key step that determines the mechanical performances and shape quality of 3D printed ceramics. In this domain, there is an increasing interest in complex thin structures and low fill density shapes. However, these complex structures may suffer from distortions by gravity forces developed on the light structure, friction with supports, shrinkage anisotropy or thermal gradients. Finite element simulation of the sintering process is then of high importance for predicting the specimens distortions. This paper focuses on the identification of the model parameters in the special case of anisotropic sintering of porcelain with final stage swelling. This study points out the printed specimen high resistance to high temperature shear deformation due to the alignment of the printed rods. A mesoscale simulation has been carried out to explain this mechanism. The resulting model was tested for the sintering of a thin wall cup shape.

Graphical Abstract

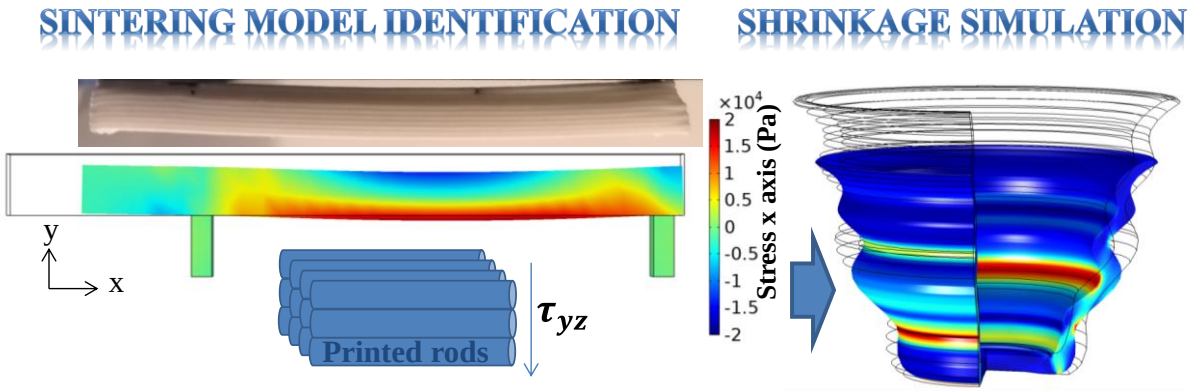

* Corresponding author: **CM**: Laboratoire de cristallographie et sciences des matériaux (CRISMAT), 6 Bvd du maréchal Juin 14050 CAEN CEDEX 4, France
Ph.: +33.2.31.45.13.69 ; *E-mail address*: charles.maniere@ensicaen.fr

Nomenclature

θ Porosity

$\dot{\theta}$ Porosity rate (s^{-1})

$\underline{\sigma}$ Stress tensor ($N.m^{-2}$)

σ_{eq} Equivalent stress ($N.m^{-2}$)

$\underline{\dot{\varepsilon}}$ Strain rate tensor (s^{-1})

$\dot{\varepsilon}_{eq}$ Equivalent strain rate (s^{-1})

$\dot{\varepsilon}_r$ Radial strain rate component (s^{-1})

$\dot{\varepsilon}_z$ Z axis strain rate component (s^{-1})

$\dot{\varepsilon}_{sintering}$ Free strain rate due to sintering (s^{-1})

φ Shear modulus

ψ Bulk modulus

θ_c Critical porosity for sintering final stage

Pl Sintering stress (Pa)

P_s Pore gas pressure in closed porosity (Pa)

$\mathbb{i}$ Identity tensor

α Surface energy ($J.m^{-2}$)

r Grain radius (m)

$\dot{e}$ Trace of the strain rate tensor (s^{-1})

η Material viscosity (Pa.s)

η_r Radial component of the viscosity (Pa.s)

η_z Z component of the viscosity (Pa.s)

η_0 Viscosity pre-exponential factor (Pa.s)

η_{0r} Radial component of the viscosity pre-exponential factor (Pa.s)

η_{0z} Z component of the viscosity pre-exponential factor (Pa.s)

Q Viscosity activation energy ($J.mol^{-1}$)

R Gas constant 8.314 ($J.mol^{-1}.K^{-1}$)

T Temperature (K)

σ_{yz} YZ stress component ($N.m^{-2}$)

1. Introduction

Ceramic 3D printing opens an interesting window for the design of high-resolution materials[1, 2] with complex structures based on multiscale/bioinspired shapes[3, 4], low density/lightweight structures[5, 6] and advanced composite structures with improved mechanical/functional properties[7, 8]. Ceramic additive manufacturing involves different methods with resolution from 0.4-1 mm for robocasting[9] (or direct write printing) to 10-100 µm for stereolithography[10]. These processes produce green specimens by extrusion and ceramic resin photopolymerization, respectively[11–13]. 3D printed green specimens are often made of low-density highly complex shapes and a complex support material network[14]. The main motivation is to obtain lightweight materials with an optimal mechanical resistance suitable for a target application[15]. However, these complex shapes are fragile all along the different processing steps, i.e. the printing, debinding and sintering. During the printing, thin shapes are very sensitive to gravity slumping. This phenomenon is controlled by the ceramic paste rheology and the printing conditions[16, 17]. The debinding is also a key step where cracks and swelling may appear if the temperature cycle is not carefully adapted to the organic phase decomposition[18, 19]. Finally, thin shapes may suffer from anisotropy[20, 21] and significant distortions[22, 23] at the sintering stage due to various causes such as gravity, friction with the support[24], high material viscosity for liquid phase sintering[25, 26], swelling (or bloating) at the final stage[27, 28] and thermal gradients[29]. Cantilever shapes without support materials are also highly sensitive to shape distortions during the sintering[30].

For selective laser melting/sintering (SLM/SLS technology), the multiphysics finite element tool is very precious to evaluate the mesoscale and macroscopic behavior of complex structures mechanical properties[31] including residual stresses, melting/sintering phenomena[32] and shrinkage issues[33, 34]. The finite element simulation of the sintering process is highly important to predict the distortion resistance of the different complex shapes

studied by 3D printing. In particular, such simulation can predict the mechanical resistance of the green specimen during its sintering, allowing adjusting the different strategies of filling density and/or the structure of the sacrificial support materials.

This work is dedicated to the sintering of 3D printed porcelain obtained by robocasting [35]. Liquid phase sintering of porcelain is a very sensitive process which requires a careful control of the cycle, in particular at the end of the sintering stage, where swelling may occur due to trapped gas in pores generating a force opposite to the capillarity sintering driving force [36]. This phenomenon is particularly important if the final stage temperature is too high[37]. However, the main phenomenon studied in the present paper is the sintering shrinkage anisotropy resulting from the extruded rods stacking strategy, printing conditions and consequently from the porosity generated[9, 38]. The impact of printing architecture, shape scale and sintering conditions on anisotropy will be investigated. The previously developed method for the identification of anisotropic behavior will be used to determine the sintering model anisotropic parameters[20]. Thereafter, the resulting model will be used in a finite element code to calibrate the viscous behavior of the printed porcelain specimen via a deflection test and a mesoscale simulation. Finally, the simulation will be used to predict the anisotropic sintering shrinkage behavior of printed complex shapes.

2. Theory and calculations

The sintering model is based on the continuum theory of sintering[39]. In the following, the sintering general equations will be defined first; then, the modeling case of sintering anisotropy in the presence of porosity will be described.

2.1. Sintering continuum model

The continuum theory of sintering defines the sintering behavior of a continuum compressible medium by the following stress and strain rate tensor equation [39, 40].

$$\underline{\sigma} = \frac{\sigma_{eq}}{\dot{\varepsilon}_{eq}}\left(\varphi\underline{\dot{\varepsilon}} + \left(\psi - \frac{1}{3}\varphi\right)\dot{e}\mathbb{i}\right) + (P_l - P_s)\mathbb{i} \quad (1)$$

The right term $P_l\mathbb{i}$ is the capillarity force resulting from sintering stress that can be expressed theoretically *via* Skorohod equation (2) [41].

$$P_l = \frac{3\alpha}{r}(1-\theta)^2 \quad (2).$$

In equation (1), the equivalent stress σ_{eq} and strain rate $\dot{\varepsilon}_{eq}$ ratio corresponds to the equivalent dense phase behavior. As pressureless sintering has low sintering stresses, the dominant sintering matter transport mechanisms are assumed to be diffusive or viscous mechanisms. These mechanisms are linear and obey linear viscous equation (3) [42].

$$\sigma_{eq} = 2\eta\dot{\varepsilon}_{eq} \quad (3).$$

For porcelain sintering which is based on liquid phase sintering (also called vitrification sintering), the mechanism is typically linear and also obeys equation (3).

The temperature dependence of the material viscosity η is typically [43]:

$$2\eta = \eta_0 T\exp(\frac{Q}{RT}) \quad (4).$$

Equation (1) general form for pressureless sintering is then:

$$\underline{\sigma} = 2\eta\left(\varphi\underline{\dot{\varepsilon}} + \left(\psi - \frac{1}{3}\varphi\right)\dot{e}\mathbb{i}\right) + (P_l - P_s)\mathbb{i} \quad (5).$$

The porosity function φ and ψ (shear and bulk modulus respectively) can also be theoretically defined *via* Skorohod's equations [39, 41]:

$$\varphi = (1-\theta)^2 \quad (6)$$

$$\psi = \frac{2}{3}\frac{(1-\theta)^3}{\theta} \quad (7).$$

In order to link the volume change rate ($\dot{\varepsilon}_x + \dot{\varepsilon}_y + \dot{\varepsilon}_z$) and the porosity elimination rate $\dot{\theta}$, the mass conservation equation is employed.

$$\frac{\dot{\theta}}{1-\theta} = \dot{\varepsilon}_x + \dot{\varepsilon}_y + \dot{\varepsilon}_z \quad (9)$$

Implementing equations (5,6,7 and 9) in a finite element code allows simulating the pressureless sintering. The main sintering parameters to determine are the following η_0/α, Q

and the initial particle radius (see details in [20]). The shear and bulk moduli may also be determined experimentally[44], however using Skorohod equations[41], porous behavior can be approximated reducing drastically the identification methodology.

$$\underline{\sigma} = 2\eta\left(\varphi\underline{\dot{\varepsilon}} + \left(\psi - \frac{1}{3}\varphi\right)\dot{\varepsilon}\underline{\underline{1}}\right) + (P_l - P_s)\underline{\underline{1}} \qquad (10).$$

2.2. Anisotropic pressureless sintering model

The 3D printing process implies a preferential interlayer porosity distribution [20, 21]. Consequently, the sintering shrinkage of the parts is rarely isotropic and may experience an anisotropic behavior. This anisotropic behavior can be inserted at the level of the viscosity η, shear and bulk moduli (ψ and φ) or sintering stress P_l. However, in opposition to the nonlinear sintering law, the linear sintering equation does not distinguish the two latter terms that are generally defined together as shear and bulk viscosity [20, 45]. Therefore, the anisotropy behavior can be inserted at the level of the viscosity (η_z, η_r) having then a different value in the layers plane (R axis) and in the normal layers direction (Z axis).

$$2\eta_r = \eta_{0r} T \exp\left(\frac{Q}{RT}\right) \qquad (11).$$

$$2\eta_z = \eta_{0z} T \exp\left(\frac{Q}{RT}\right) \qquad (12).$$

The anisotropic model parameters can be identified by adjusting the simulated sintering response to the dilatometry specimen diameter and height to obtain: η_{0r}, η_{0z} and Q. The finite element simulation code employed was Comsol Multiphysics.

3. Experiment and method

This study is divided in three main stages including (i) the modeling parameters identification from dilatometry (ii) the correction of the model based on deflection sintering tests combined with the simulation tool and (iii) the final comparison of the resulting modeling approach on a complex shape.

3.1. Samples preparation

The sintering dilatometry tests were conducted on the apparatus “Setaram TMA92” with 3D printed porcelain cut in 6.7 mm height and 5.7 mm diameter specimens. The robocasting 3D printing method was based on “delta wasp 2040 clay”. An aqueous porcelain ceramic paste consisting of “CERADEL PT010B” with 5 % of water addition was used for the robocasting process with the following printing conditions: print speed 50mm/s, nozzle size 1.2 mm, extrusion gas pressure 4 bar, layer height 0.5 mm, bottom/top thickness 2 mm, shell thickness 2.4 mm, filling density 100 %. In a previous article [46], a dilatometric study was carried out showing the swelling phenomenon and allowing to determine an optimum sintering cycle providing high density while minimizing the pore gas pressure swelling phenomenon. This cycle is 1K/min to 1200°C with 2h holding. This thermal cycle has been used for all the experiments of this study, including for the dilatometric measurements. In order to determine the anisotropic sintering shrinkage magnitude for different experimental parameters, three runs of tests were done to investigate the effect of sintering heating rates, volume and filling ratio. The identification of the sintering parameters using equations (11 and 12) will be done by the adjustment of the specimen dimensions.

3.2. Bar deflection tests and anisotropic simulation

In order to test and adjust the sintering parameters identified by dilatometry, the numerical tool is first compared to a bar deflection test. The latter dimensions are 6 × 6 × 60 mm. The bar is placed on the top of an alumina cup with a 45 mm inner diameter for allowing the specimen slumping during sintering. The configuration is presented in figure 1a. Figure 1b illustrates the distortion after the sintering (1K/min to 1200°C, 2h holding). A deflection of 0.5 mm is observed. This experimental deflection will be compared to the finite element simulation result.

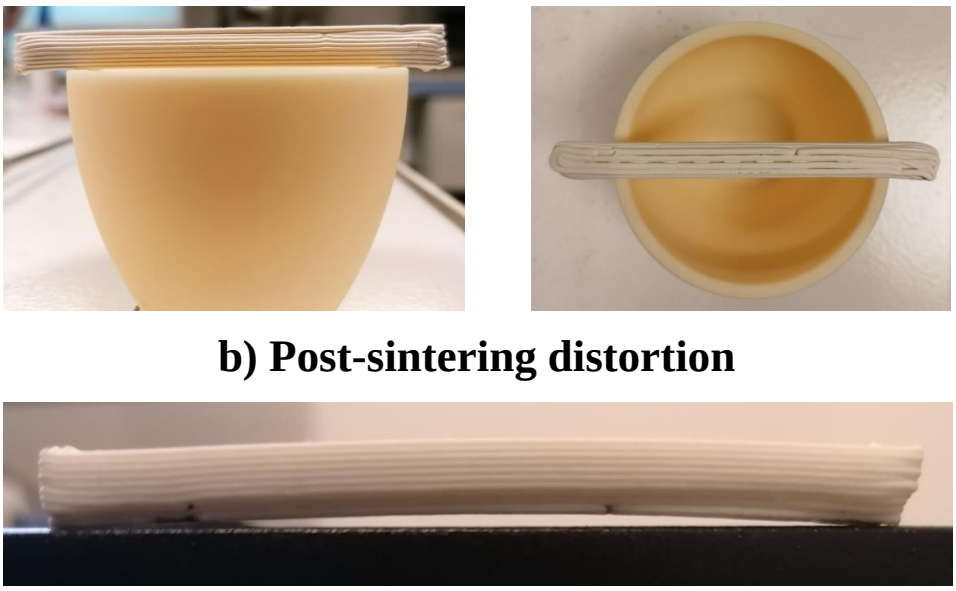

Figure 1 Bar deflection sintering test, a) configuration before sintering, b) lateral view of the sintered specimen.

3.3. Cup shape sintering simulation

After the calibration of the finite element sintering model from dilatometry and deflection tests, the sintering of a complex shape is studied to estimate the accuracy of the simulation tool on real objects. Two cup shape specimens are investigated with different dimensions to test the scale effect on sintering and the capacity of the numerical tool to predict the final shape dimensions. The smaller sample external dimensions are 32 mm height × 23 mm radius and the larger specimen, 60 mm height × 42 mm radius. These dimensions correspond to the dry printed shapes. The same dilatometry temperature cycle is imposed (1K/min to 1200°C, 2h holding). Simulations are conducted using COMSOL Multiphysics software (version 5.5), with the “nonlinear materials” module to implement the sintering behavior.

4. Results and discussions

4.1. Sintering anisotropy characterization

Figure 2 shows the results of the post-sintering anisotropy study. The anisotropy is characterized by measuring the ratio of the final and initial height and diameter. If the sintering is isotropic, the ratio hf/hi and df/di must be the same, and different if anisotropic shrinkage occurs. In a previous study [46], sintering with different heating rates has been explored by dilatometry on the "10 mm" specimens. The results presented in figure 2a, show an anisotropic shrinkage behavior with hf/hi close to 0.83 and df/di close to 0.9. The heating rate does not have any noticeable impact on these ratios. Very similar results are obtained for the scalability and filling ratio tests illustrated in figure 2b and figure 2c respectively. Bigger specimens and high void ratios in the volume of the specimen do not generate significant differences in the anisotropy behavior. In overall, the average hf/hi ratio is 0.89 ± 0.01 and df/di ratio is 0.82 ± 0.01. This reproducibility of the anisotropic sintering shrinkage indicates the latter must be originated from the layered printing conditions rather than the heating cycle, the specimen size or its architecture (filling ratio). This means that the sintering shrinkage can be predicted by the finite element simulation after a careful identification of the anisotropic sintering conditions. In below section the identification process begins with the dilatometry test.

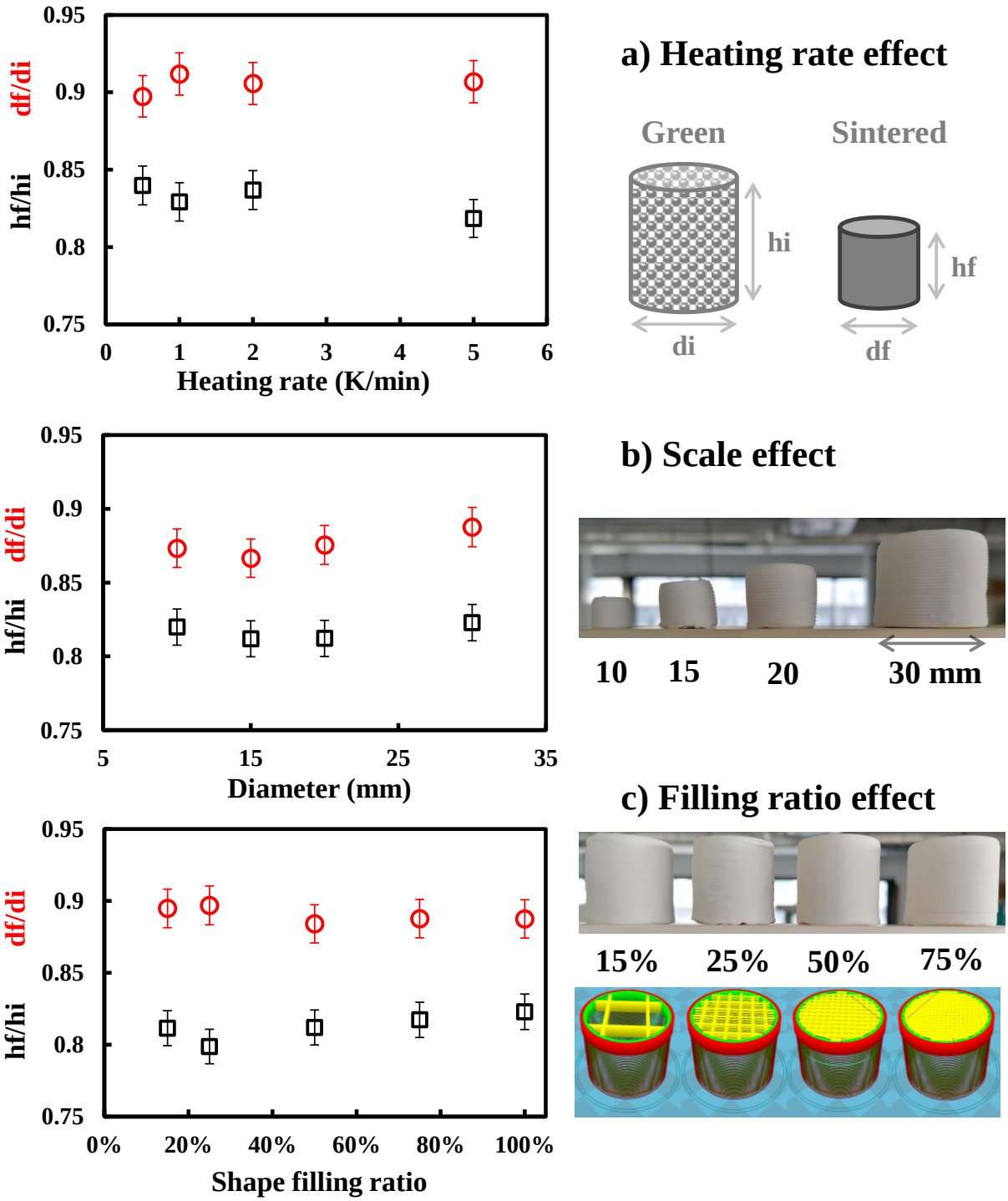

Figure 2 Sintering anisotropy parametric analysis: a) effect of heating rate of 10 mm specimens, b) scale effect on specimens with diametric homothetic increase from 10 to 30 mm, c) filling ratio effect on 30 mm diameter samples, the filling architecture is shown on lower right by the yellow walls in the volume of the parts.

4.2. Determination of the sintering model anisotropic parameters

The sintering cycle, height, diameter and porosity of the dilatometry test are shown in figure 3. These experimental sintering data are used to adjust the sintering model that will

reproduce these anisotropic sintering responses. As a starting point, the isotropic model parameters employed in ref[46] will be used and modified to reproduce the anisotropic behavior. Two modeling approaches are investigated; one will consider the trapped gas pressure in the closed pores at the final stage [46] and will be referred as "pore gas pressure model". The other modeling approach will consist in the use of a threshold law on the bulk modulus (11) to explain the sintering slowdown at the final stage (by a critical porosity θ_c) instead of considering the trapped gas pressure in pores. This approach will be referred as "threshold model".

$$\psi = \frac{2}{3}\frac{(1-\theta)^3}{(\theta-\theta_c)} \qquad (11).$$

The two sintering models are reported in figure 3 after the adjustment of their parameters. Both succeed to reproduce the sintering response of the printed sample and have in common the activation energy of 300.3 kJ/mol and $\eta_{0z} = 3.00E-3\ Pa.s$. Then, the "pore gas pressure model" considers the function P_s determined in ref[46], the shear modulus expression (7) and:

$$\eta_{0r} = \eta_{0z} + 0.001\theta^{2.5} \qquad (12).$$

The porosity function in the expression of η_{0r} is a variable tending to zero at full density. The latter function gradually suppresses the anisotropy behavior as the porosity decreases. This function considers the porosity distribution (higher interface porosity) as the origin of the anisotropic behavior. Consequently, at full density, the anisotropic model tends to a pure isotropic creep model[20].

The "threshold model" considers a critical porosity of $\theta_c = 0.068$ in the bulk modulus equation (11), $P_s = 0$ and:

$$\eta_{0r} = \eta_{0z} + 0.00021(\theta - 0.068)^{2.7} \qquad (13).$$

We can note the porosity expression of η_{0r} also has a critical porosity because the underlying hypothesis of the "threshold model" is the presence of large size and stable pores at the final stage. With such hypothesis the anisotropy should vanish when these stable pores appear.

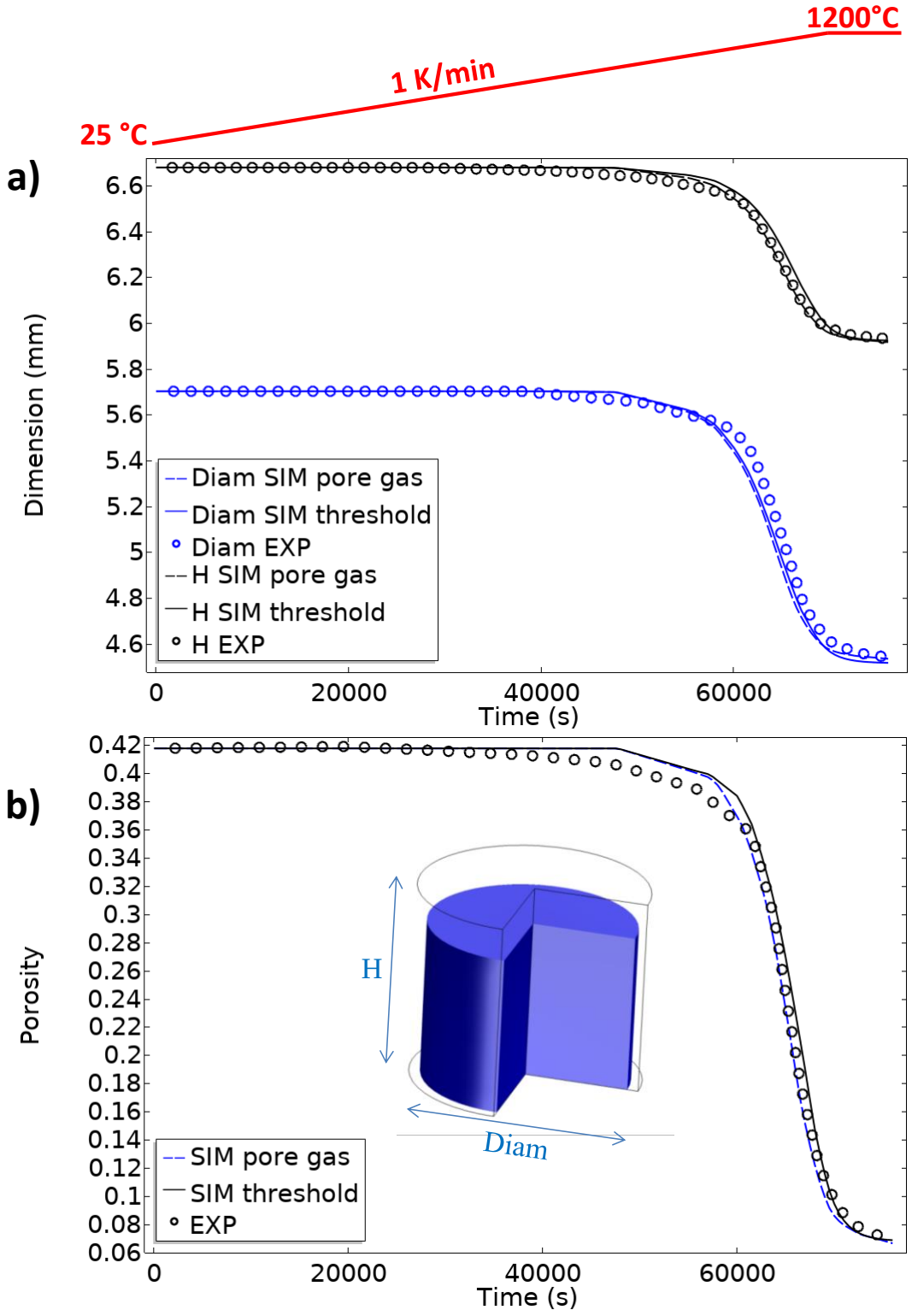

Figure 3 Sintering model identification from dilatometry tests, a) adjustment of the modeled specimen diameter and height, b) experimental and modeled porosity.

4.3. Simulation of the sintering deflection test

In this section, the “pore gas pressure model” and “threshold model” are tested on the deflection case; the results are shown in figure 4. The two lateral supports correspond to the alumina cup edge represented in figure 1a. In these simulations the stress developed along the bar direction is in tension below the bar and in compression on the upper part. However, the model identified by dilatometry (1X) predicts an excessive deflection compared to the experiment (0.5 mm). This difference is supposed to be attributed to the preferential orientation of the extruded rods along the bar while typical printed samples in figure 2 are a sequence of layers with different rod orientations. In order to slow the creep deformation behavior while keeping the anisotropic sintering behavior unchanged, one way is to modify exclusively the shear creep viscosity by an amplification factor. By doing so, only the shear components are affected without modifying the diagonal term of the tensors component in equation (10). The first observation of figure 4 is that a high amplification factor is required to significantly slow down the shear deformation. In the “pore gas pressure model” the effect is very limited, only the “threshold model” seems to efficiently react to this additional factor. In order to find the optimum shear factor, the modeled deflection results have been plotted in figure 5a. The optimum factor is 44, the corresponding simulation is reported in figure 5b with (as comparison) the lateral view of the bar deflection test showing similar deflection levels. At this stage we obtain a model reproducing the anisotropic sintering response and the high creep resistance of preferential rods orientation in bars shapes. However, the reason for this high creep resistance is questioning and in the next section, we will explore two possible reasons for this creep resistance by mesoscale simulations.

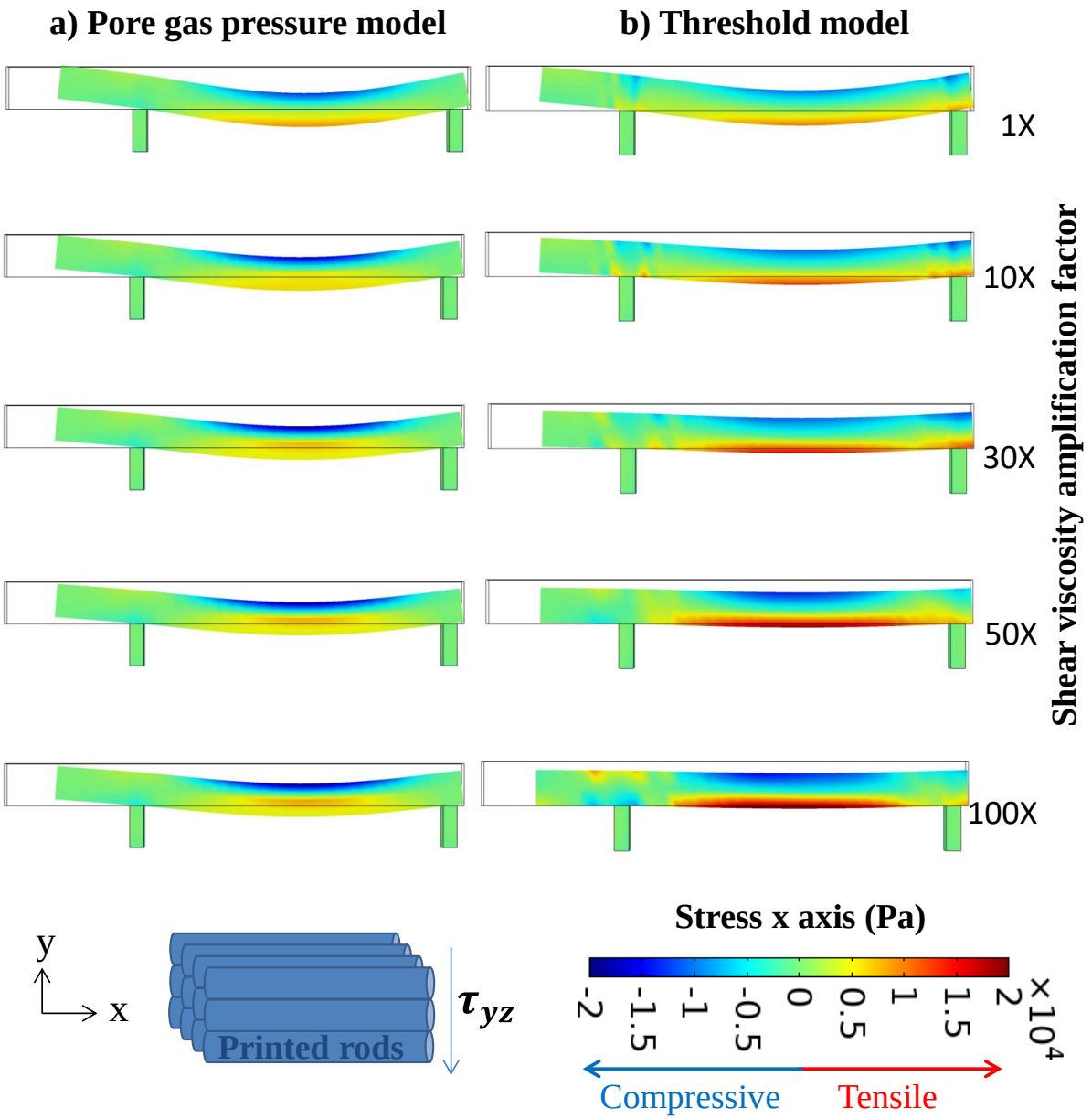

Figure 4 Modeling of the sintering deflection test by pore gas (a) and threshold (b) approaches, the creep based deflection magnitude has been modified via a parametric study on the shear viscosity terms.

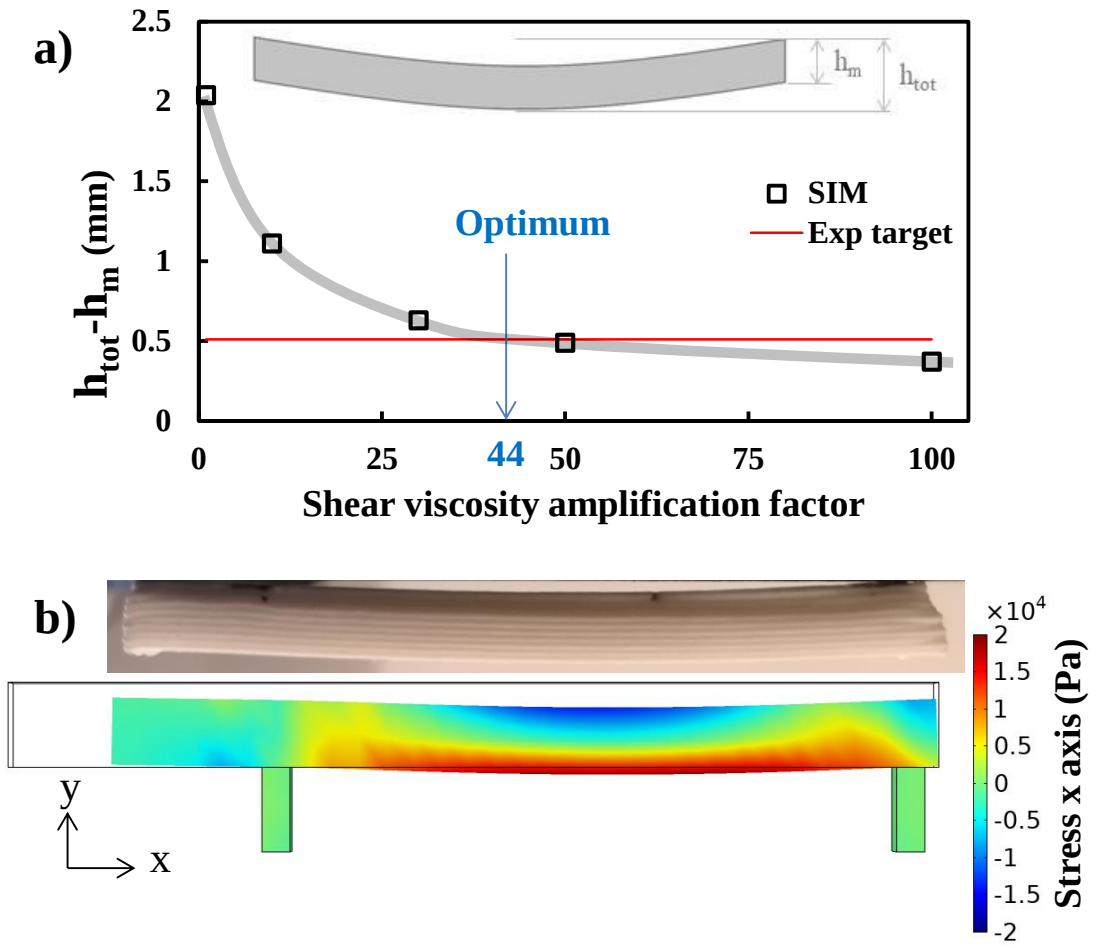

Figure 5 a) Deflection curves for different shear viscosity factors, b) experimental vs optimum sintering simulation for the bar post-sintering deformation.

4.4. Mesoscale sintering simulation

Before simulating the creep behavior at the microstructure level, a careful analysis of the sintered porcelain microstructure is required. The optical microscopy and EDS mapping of the polished sample are reported in figure 6a and b. The microstructure is homogeneous as shown in figure 6c. Vitrification is the mechanism by which porcelain sintering occurs: the microstructure typically shows an important proportion of glass phase with multimodal porosity size and the presence of large silica particles trapped in the glassy phase. In the EDS map of Al, Si elements on figure 6b, the silica phase appears in green, the mixed violet/green area is the glassy phase, and black zones are porosity. As highlighted in the previous paper [46], the sintering of this material suffers from a swelling phenomenon which induces an important pore growth in the interlayer zone. From this microstructure observation, two

origins for the creep resistance will be explored. On one hand, the align rods and the close pore gas pressure at the interlayer may implicate a higher effective consistency in shear solicitation. On the other hand, the silica large particles preferentially oriented in the extrusion direction (see figure 6b) may also increase the effective shear viscosity by playing a similar role than rigid inclusions.

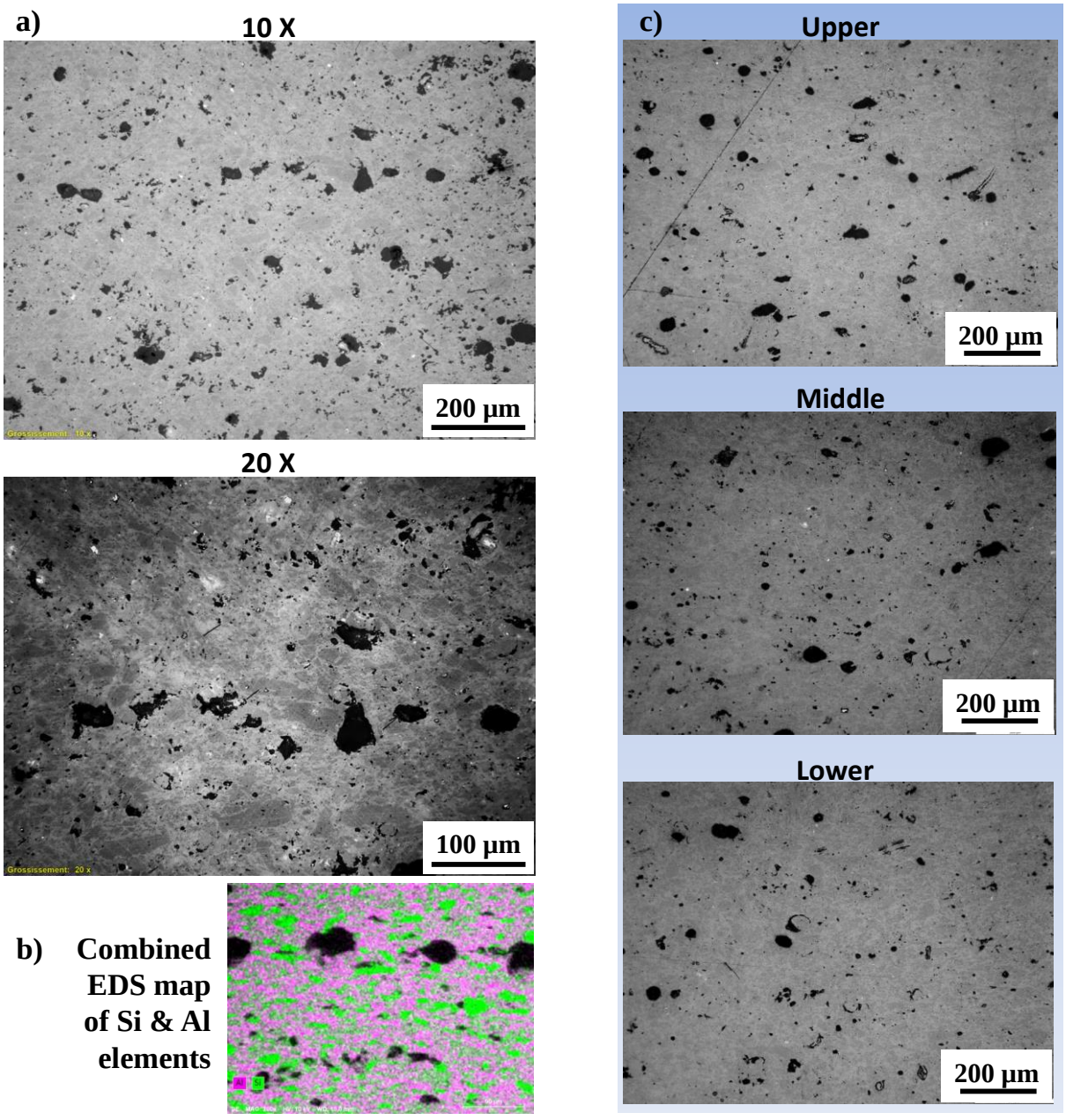

Figure 6 a) Optical microscopy of the sintering specimen microstructure, b) Al, Si elements EDSmap of the latter microstructure c) microstructure at the upper, middle, and lower part of a 10 mm diameter sintered specimen.

These two approaches will be tested in a mesoscale simulation with the aim of testing the magnitude of both hypotheses on the effective viscosity amplification. As represented in figure 7a, the mesoscale simulation is built as a virtual shear test at microstructure level. For neglecting the densification effect, the porosity of the bulk is taken to the value of 0.1, a value close to the overall porosity at the beginning of the holding where the deflection phenomenon is active. In this shear configuration, the shear creep strain rate expression is:

$$\dot{\varepsilon}_{yz} = \frac{1}{2\eta}\frac{\sigma_{yz}}{\varphi} \qquad (14).$$

The sliding velocity v_g is related to the strain rate by:

$$\dot{\varepsilon}_{yz} = \frac{|v_g|}{2e} \qquad (15).$$

The effective viscosity is then calculated by:

$$\eta = \frac{e}{|v_g|}\frac{\sigma_{yz}}{\varphi} \qquad (16).$$

In the simulation illustrated in figure 7, the effect of the interlayer higher porosity is tested. The thickness of the layer and interlayer porous zone has been determined by the microstructure on figure 6a. The shear displacement is shown in figure 7b ; the term $-P_l+P_{gas}$ can be assimilated to the effective sintering stress. The latter has a negative value when the curvature capillarity forces dominate (densification) and a positive value when trap gas pressure dominates (swelling). With the chosen porosity, the mesoscale simulation (figure 7b) predicts a situation of swelling in the interlayer region and densification in the layer bulk. This situation is very close to the microstructure seen on figure 6 with large pores at the interfaces. This particular situation allows the layer to slide over each other and generates a highly effective shear viscosity more than ten times the bulk viscosity (figure 7c). The local maximum at 1200 s in figure 7c seems to correspond to the onset of intense swelling ($P_l<<P_{gas}$ and significant increase of the porous layer thickness).

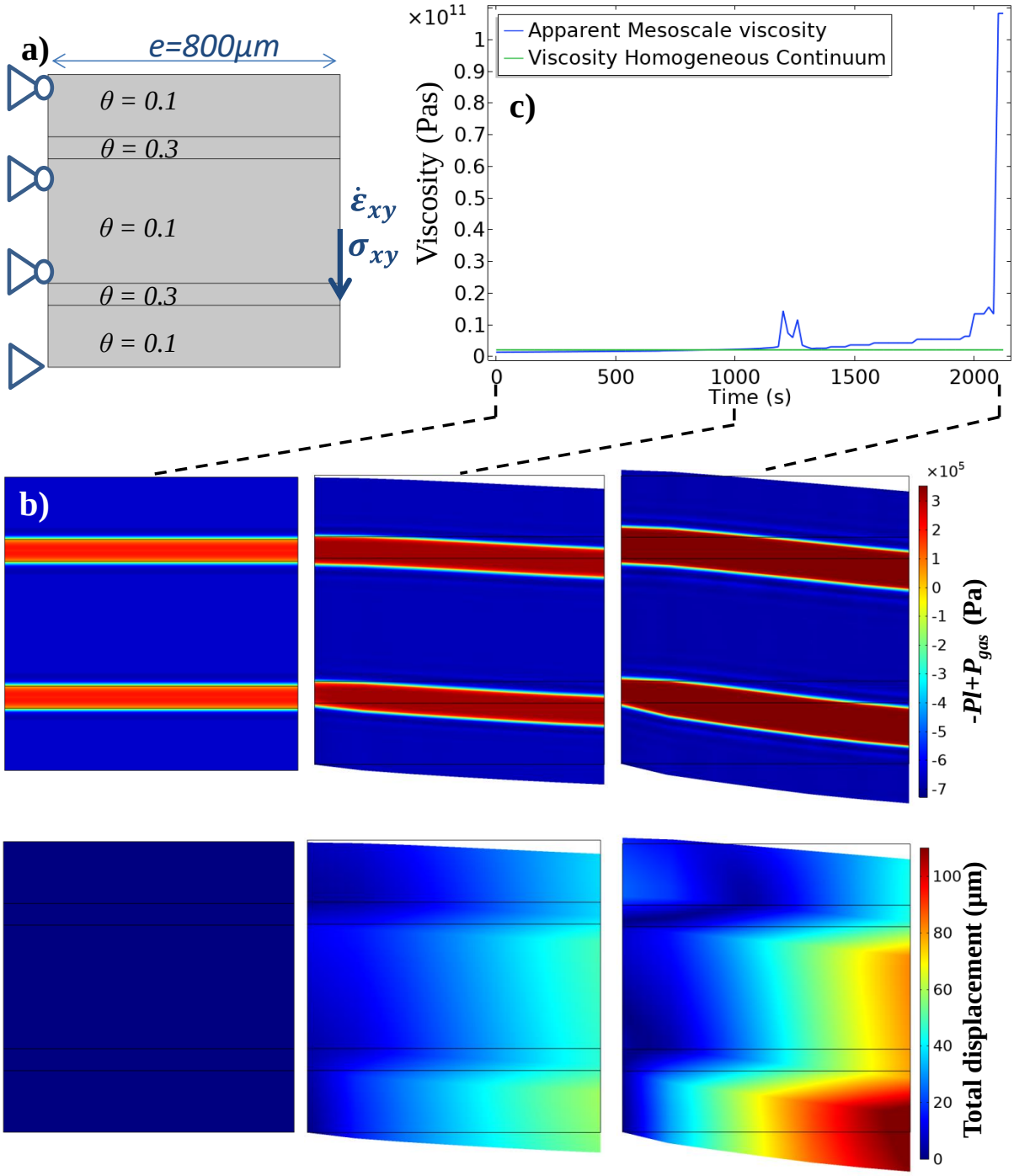

Figure 7 Mesoscale simulation of the layered microstructure assuming pore gas pressure and lower porosity in the layers interfaces, a) microstructural model structure, b) mesoscale simulated images of the shear deformations and effective sintering stress ($-P_l+P_{gas}$), c) simulated apparent shear viscosity vs continuum viscosity.

In figure 8a, the presence of SiO_2 rigid inclusion is tested. The simulation with 25% of SiO_2 was based on the microstructure illustrated on figure 6a. Higher contents are also tested. The shear effective viscosity is reported in figure 8b, with in figure 8c the shear deformations. In this approach, we assume that the bulk viscosity is similar to the effective viscosity of the

glassy phase responsible for sintering densification. For the 25%, the amplification of the effective viscosity is only twice the bulk. However, assuming the SiO_2 is partially dissolved into the glassy phase during sintering, the zone of rigid influence may be higher. Therefore a higher content of SiO_2 may also be considered even if their amplification influence on the effective viscosity is only five times the bulk viscosity. This mesoscale simulation shows the effective viscosity for creep deformation may be higher than the effective viscosity calculated from the sintering phenomenon. Both SiO_2 inclusions and interlayer structure swelling may play a role in the creep resistance experimentally observed.

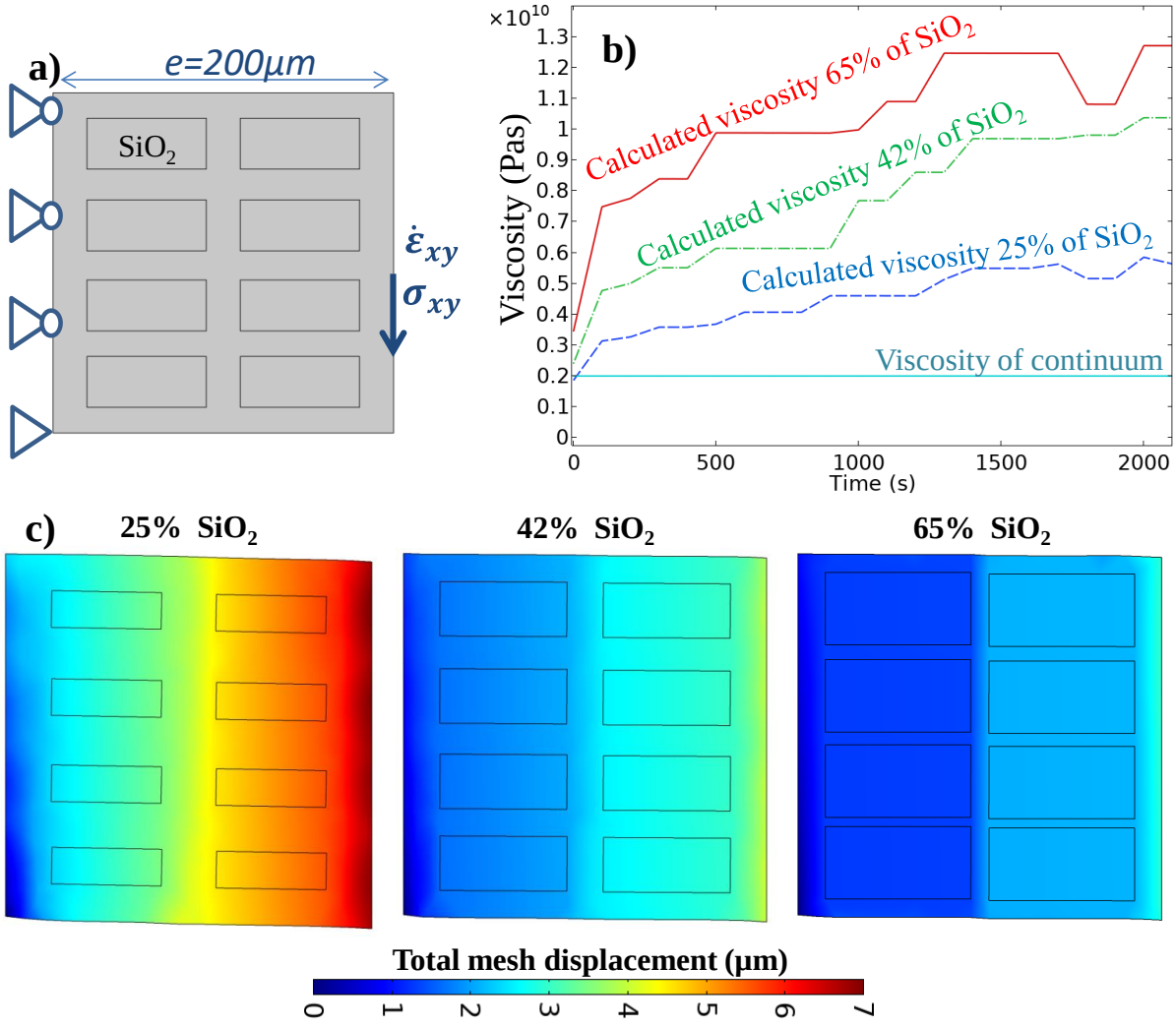

Figure 8 Mesoscale simulation of the layered microstructure assuming SiO_2 rigid inclusions, a) microstructural model structure, b) simulated apparent shear viscosity vs continuum viscosity for different content of SiO_2, c) mesoscale simulated images of the shear deformations.

4.5. Cup shape experimental/numerical comparison

The first aspect to take into account for modeling the cup shapes sintering from green state is the drying step that modifies the 3D design dimensions. Without a 3D scanner or a numerical simulation tool able to predict the drying stage, a correction on the height and radial dimension was applied to match the green shape dimensions from the printed CAD (Computer Aid Design) shapes. The dimensions of the green printed cups were measured accordingly to the scheme on figure 9a (r_1,r_2,r_3,r_4 and h). In figure 9bc, the radial dimensions of the cup were fitted with a polynomial function allowing applying the radial dry shape correction to the FEM green shape. In the same way, the vertical dimensions of the CAD file were corrected based on the cup height information. This approach is not ideal as not all the dry radial dimensions matched (only two of them are approached).

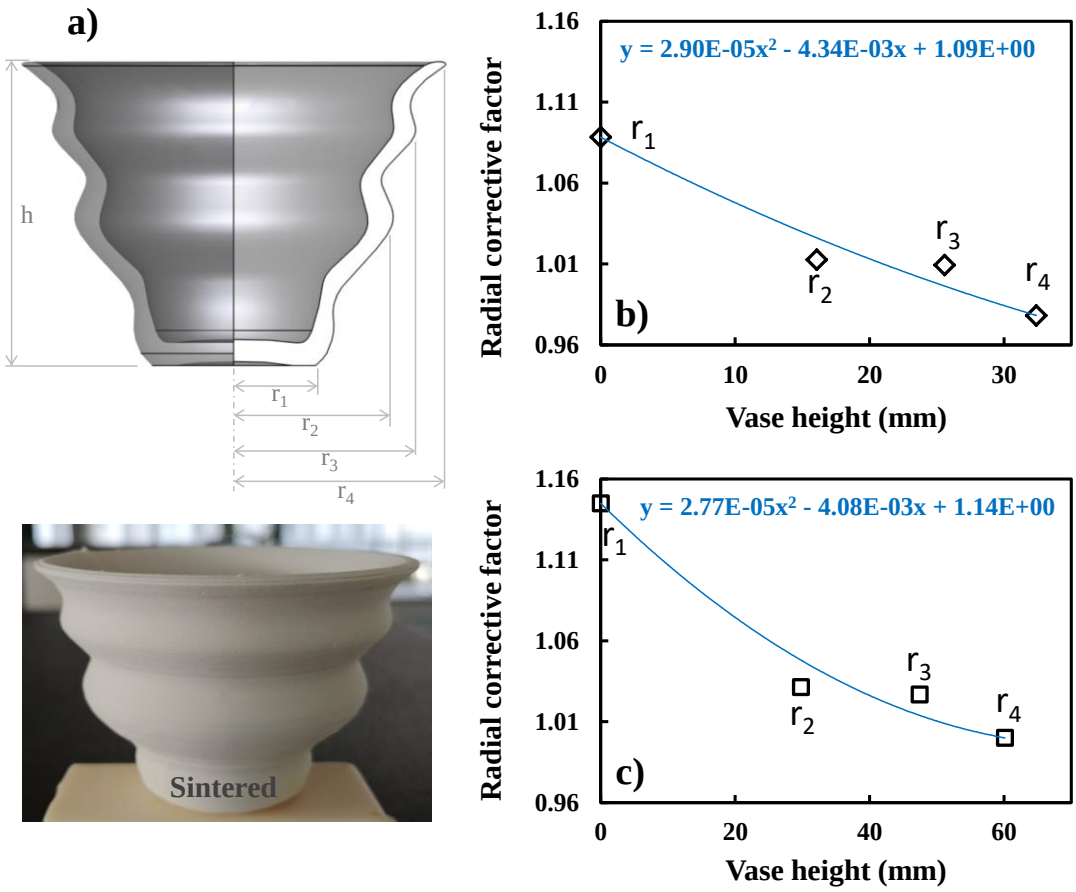

Figure 9 a) Cup shape main reference dimensions, b,c) experimental radial corrective factor vs cup height to assumes the shape drying shrinkage on the initial simulated geometry for the small cup (b) and large cup (c).

The results of the simulation of the small and large cups by “pore gas pressure” and “threshold” approach are illustrated in figure 10ab. For the “threshold” approach, the shear viscosity amplification factor (44) was taken into account for the lateral parts of the shape (without the support) because this zone has a preferential orientation like for the bar shape (figure 4b). The simulation figure 10ab shows the stress developed in the shape by the action of its own weight. As expected, the stress is higher for the large cup. The internal stress is concentrated in the zone “r2” (see figure 9a). This zone has a cantilever shape and supports the weight of the upper part. If the wall thickness had been thinner in this area (like for lattice structures), a distortion could have happened.

In figure 10c, the experimental/simulated dimensions of the green sintered and simulated sintered shapes are compared. The ratio of the final and initial dimensions (df/di) highlights the anisotropic behavior. The dimensions of the two simulation approaches are very close; the error is in most cases below 5%. For the small cup, a higher error close to 8% is noted and can be explained by the lower experimental anisotropy of this small cup shape. It is possible that the thin wall of this shape implies a different extruded rod distribution and then a different sintering behavior.

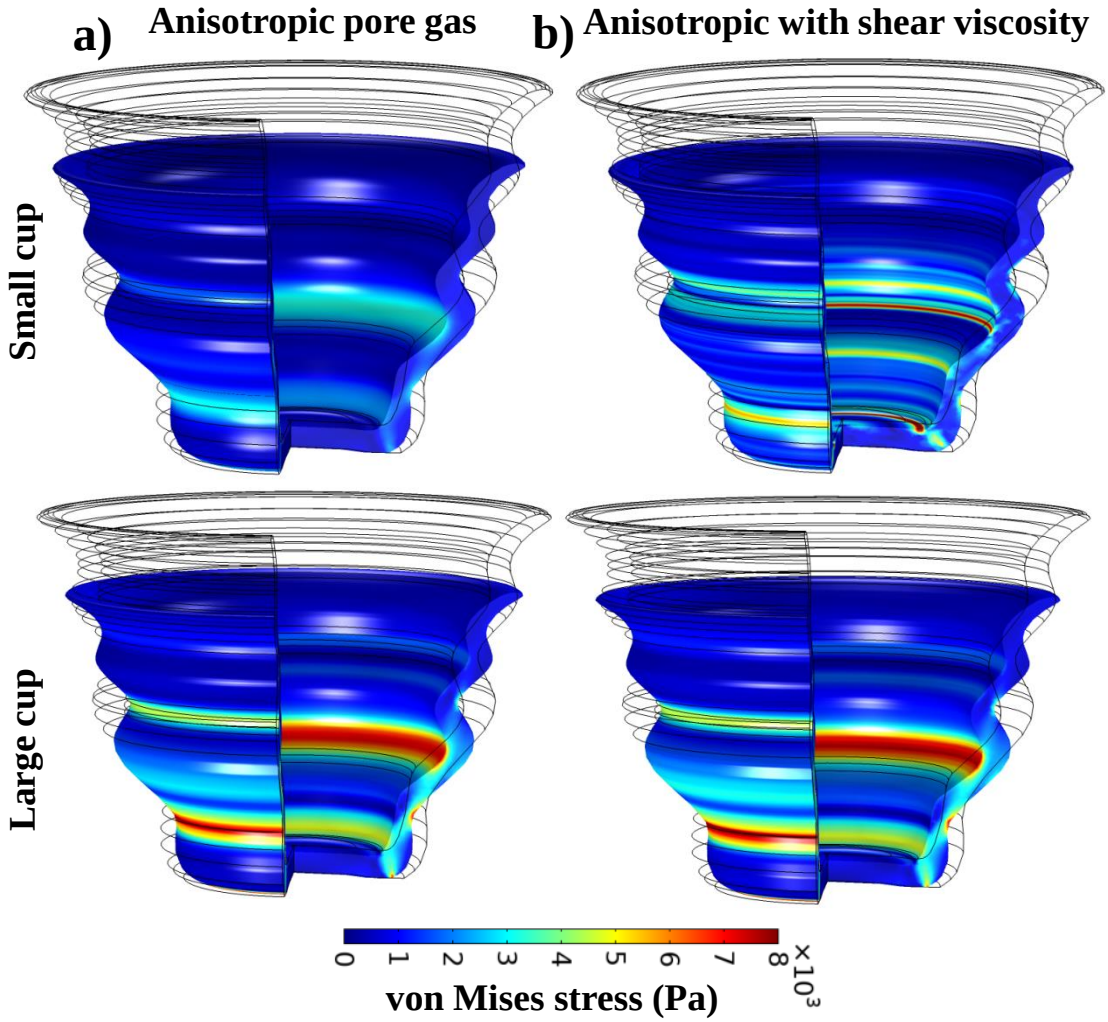

Figure 10 Simulated small and large cup sintering with pore gas model (black lines correspond to the green shape dimensions) (a) and the threshold approach with shear viscosity correction (b).

Table 1 Simulation/experiment dimensions comparison

		Green body	Sintered EXP	df / di EXP	Sintered SIM with pore gas	Sintered SIM with SHEAR
Small Cup	**h**	32.74	28.24	0.86	25.78	25.92
	r_1	9.88	8.68	0.88	8.74	8.75
	r_2	18.18	16.16	0.89	16.38	16.39
	r_3	20.66	18.53	0.90	18.10	18.12
	r_4	23.32	20.82	0.89	20.70	20.71
Large Cup	**h**	60.74	49.23	0.81	47.80	47.38
	r_1	18.41	15.90	0.86	16.30	16.24
	r_2	32.81	29.40	0.90	29,82	29.7
	r_3	37.21	33.30	0.90	32.75	32.64
	r_4	42.22	38.14	0.90	37.69	37.54

5. Conclusion

In this study, a comprehensive simulation method of robocasted ceramic sintering has been presented. This approach encompasses the identification of the anisotropic sintering behavior, the adjustment of the sintering model *via* deflection sintering tests, and the finite element simulation of a complex shape. The aim of this study is to establish a methodology able to simulate the sintering of 3D printed ceramic object. This numerical tool is required to predict at the design stage the shape distortions of the sintering stage. This modeling approach is aimed at helping the design of the shapes and supports at the conception stage for production purpose. The following points are highlighted:

- The anisotropic sintering model can be identified by the adjustment of dilatometry and deflection sintering tests. The sintering behavior and creep deformation at high temperature are determined experimentally by this method.
- The model can take into account late stage sintering swelling phenomena and the shrinkage anisotropy originated from a heterogeneous porosity distribution during the printing.
- The printed specimens have a layered structure implying a noticeable creep deformation resistance at high temperature. The deflection test showed a very limited deformation. From mesoscale simulations, this phenomenon may be explained by a combination of SiO_2 particle acting like rigid inclusions and the trap gas pressure in the interlayer area generating a localized layered stress field.
- The simulation tool predicts the sintering shrinkage with precision below 5%. A discrepancy is noted on printed shapes with a thin wall probably due to a different printing layered structure at the edges.

Acknowledgements

The help and support of Jérôme Lecourt and Christelle Bilot is gratefully acknowledged.

Credit authorship contribution statement

Charles Manière: Conceptualization, Supervision, Modeling, Writing; **Christelle Harnois:** Conceptualization, review & editing; **Sylvain Marinel:** Conceptualization, Supervision, review & editing.

Funding

No funding

Data availability

All data is published with the paper.

Compliance with ethical standards

Conflict of interest: The authors declare that they have no conflict of interest.

Consent to participate: No human or animal was involved in this work; thus, no consent was required.

Consent to publish: All authors have given their permission for publishing this work.

Code availability: The simulation software Comsol Multiphysics 5.5 is a commercially licensed product of Comsol Corporation.

References

1. Chartier T, Duterte C, Delhote N, et al (2008) Fabrication of Millimeter Wave

Components Via Ceramic Stereo- and Microstereolithography Processes. J Am Ceram Soc 91:2469–2474. https://doi.org/10.1111/j.1551-2916.2008.02482.x

2. Deubel M, von Freymann G, Wegener M, et al (2004) Direct laser writing of three-dimensional photonic-crystal templates for telecommunications. Nat Mater 3:444–447. https://doi.org/10.1038/nmat1155
3. Li Y, Mao H, Hu P, et al (2019) Bioinspired Functional Surfaces Enabled by Multiscale Stereolithography. Adv Mater Technol 4:1800638. https://doi.org/10.1002/admt.201800638
4. Yang Y, Li X, Zheng X, et al (2018) 3D-Printed Biomimetic Super-Hydrophobic Structure for Microdroplet Manipulation and Oil/Water Separation. Adv Mater 30:1704912. https://doi.org/10.1002/adma.201704912
5. He L, Fei F, Wang W, Song X (2019) Support-Free Ceramic Stereolithography of Complex Overhanging Structures Based on an Elasto-viscoplastic Suspension Feedstock. ACS Appl Mater Interfaces 11:18849–18857. https://doi.org/10.1021/acsami.9b04205
6. Li Z, Chen Z, Liu J, et al (2020) Additive manufacturing of lightweight and high-strength polymer-derived SiOC ceramics. Virtual Phys Prototyp 15:163–177. https://doi.org/10.1080/17452759.2019.1710919
7. Zhang H, Yang Y, Hu K, et al (2020) Stereolithography-based additive manufacturing of lightweight and high-strength Cf/SiC ceramics. Addit Manuf 34:101199. https://doi.org/10.1016/j.addma.2020.101199
8. Feilden E, Ferraro C, Zhang Q, et al (2017) 3D Printing Bioinspired Ceramic Composites. Sci Rep 7:13759. https://doi.org/10.1038/s41598-017-14236-9
9. Peng E, Zhang D, Ding J (2018) Ceramic Robocasting: Recent Achievements, Potential, and Future Developments. Adv Mater 30:1802404. https://doi.org/10.1002/adma.201802404
10. Chartier T, Badev A (2013) Rapid Prototyping of Ceramics. In: Handbook of Advanced Ceramics. Elsevier, pp 489–524
11. Chen Z, Li Z, Li J, et al (2019) 3D printing of ceramics: A review. J Eur Ceram Soc 39:661–687. https://doi.org/10.1016/j.jeurceramsoc.2018.11.013
12. Deckers J, Vleugels J, Kruth JP (2014) Additive Manufacturing of Ceramics: A Review. J Ceram Sci Technol 5:245–260. https://doi.org/10.4416/JCST2014-00032
13. Wang J-C, Dommati H, Hsieh S-J (2019) Review of additive manufacturing methods for high-performance ceramic materials. Int J Adv Manuf Technol 103:2627–2647. https://doi.org/10.1007/s00170-019-03669-3

14. Jiang J, Xu X, Stringer J (2018) Support Structures for Additive Manufacturing: A Review. J Manuf Mater Process 2:64. https://doi.org/10.3390/jmmp2040064
15. Du X, Fu S, Zhu Y (2018) 3D printing of ceramic-based scaffolds for bone tissue engineering: an overview. J Mater Chem B 6:4397–4412. https://doi.org/10.1039/C8TB00677F
16. Miyanaji H, Orth M, Akbar JM, Yang L (2018) Process development for green part printing using binder jetting additive manufacturing. Front Mech Eng 13:504–512. https://doi.org/10.1007/s11465-018-0508-8
17. M'Barki A, Bocquet L, Stevenson A (2017) Linking Rheology and Printability for Dense and Strong Ceramics by Direct Ink Writing. Sci Rep 7:6017. https://doi.org/10.1038/s41598-017-06115-0
18. Bae C-J, Halloran JW (2011) Influence of Residual Monomer on Cracking in Ceramics Fabricated by Stereolithography. Int J Appl Ceram Technol 8:1289–1295. https://doi.org/10.1111/j.1744-7402.2010.02578.x
19. Li H, Song L, Sun J, et al (2019) Dental ceramic prostheses by stereolithography-based additive manufacturing: potentials and challenges. Adv Appl Ceram 118:30–36. https://doi.org/10.1080/17436753.2018.1447834
20. Manière C, Kerbart G, Harnois C, Marinel S (2020) Modeling sintering anisotropy in ceramic stereolithography of silica. Acta Mater 182:163–171. https://doi.org/10.1016/j.actamat.2019.10.032
21. Tarabeux J, Pateloup V, Michaud P, Chartier T (2018) Development of a numerical simulation model for predicting the curing of ceramic systems in the stereolithography process. J Eur Ceram Soc 38:4089–4098. https://doi.org/10.1016/j.jeurceramsoc.2018.03.052
22. Withell A, Diegel O, Grupp I, et al (2011) Porous ceramic filters through 3D printing. In: Innovative Developments in Virtual and Physical Prototyping. CRC Press, pp 313–318
23. Ohji T (2018) Additive manufacturing of ceramic components. Synthesiology 11:81–93. https://doi.org/10.5571/synth.11.2_81
24. Alvarado-Contreras JA, Olevsky EA, German RM (2013) Modeling of gravity-induced shape distortions during sintering of cylindrical specimens. Mech Res Commun 50:8–11. https://doi.org/10.1016/j.mechrescom.2013.02.007
25. Alvarado-Contreras JA, Olevsky EA, Maximenko AL, German RM (2014) A continuum approach for modeling gravitational effects on grain settling and shape distortion during liquid phase sintering of tungsten heavy alloys. Acta Mater 65:176–

184. https://doi.org/10.1016/j.actamat.2013.10.059

26. Shanshan Z, Hadi M, Li Y, et al (2014) An Experimental Study of Ceramic Dental Porcelain Materials Using A 3D Print (3DP) Process. In: Conference: 2014 Annual International Solid Freeform Fabrication Symposium (SFF Symp 2014), At Austin, TX, USA. pp 991–1011
27. Riley CM (1951) Relation of Chemical Properties to the Bloating of Clays. J Am Ceram Soc 34:121–128. https://doi.org/10.1111/j.1151-2916.1951.tb11619.x
28. Manière C, Saccardo E, Lee G, et al (2018) Swelling negation during sintering of sterling silver: An experimental and theoretical approach. Results Phys 11:79–84. https://doi.org/10.1016/j.rinp.2018.08.035
29. Manière C, Zahrah T, Olevsky EA (2017) Fluid dynamics thermo-mechanical simulation of sintering: Uniformity of temperature and density distributions. Appl Therm Eng 123:603–613. https://doi.org/10.1016/j.applthermaleng.2017.05.116
30. Lynnora O G, Magdi B A, Reid J C, et al (2018) Mitigating Distortion during Sintering of Binder Jet Printed Ceramics. In: Conference: Solid Freeform Fabrication Symposium 2018. pp 135–142
31. Eshraghi S, Das S (2012) Micromechanical finite-element modeling and experimental characterization of the compressive mechanical properties of polycaprolactone–hydroxyapatite composite scaffolds prepared by selective laser sintering for bone tissue engineering. Acta Biomater 8:3138–3143. https://doi.org/10.1016/j.actbio.2012.04.022
32. Chen Q, Guillemot G, Gandin C-A, Bellet M (2017) Three-dimensional finite element thermomechanical modeling of additive manufacturing by selective laser melting for ceramic materials. Addit Manuf 16:124–137. https://doi.org/10.1016/j.addma.2017.02.005
33. Gajera HM, Dave KG (2018) Experimental investigation and optimization of direct metal laser sintering process for shrinkage rate using CL50WS material. Mater Today Proc 5:19126–19135. https://doi.org/10.1016/j.matpr.2018.06.266
34. Fotovvati B, Asadi E (2019) Size effects on geometrical accuracy for additive manufacturing of Ti-6Al-4V ELI parts. Int J Adv Manuf Technol 104:2951–2959. https://doi.org/10.1007/s00170-019-04184-1
35. Yu T, Zhang Z, Liu Q, et al (2020) Extrusion-based additive manufacturing of yttria-partially-stabilized zirconia ceramics. Ceram Int 46:5020–5027. https://doi.org/10.1016/j.ceramint.2019.10.245
36. Sánchez E, García-Ten J, Sanz V, Moreno A (2010) Porcelain tile: Almost 30 years of steady scientific-technological evolution. Ceram Int 36:831–845.

https://doi.org/10.1016/j.ceramint.2009.11.016
37. Martín-Márquez J, Rincón JM, Romero M (2008) Effect of firing temperature on sintering of porcelain stoneware tiles. Ceram Int 34:1867–1873. https://doi.org/10.1016/j.ceramint.2007.06.006
38. Chartier T, Pateloup V, Chaput C (2018) Manufacturing of ceramic parts by additive manufacturing technologies. Tech l'ingénieur N4807v1:1–27
39. Olevsky EA (1998) Theory of sintering: from discrete to continuum. Mater Sci Eng R Reports 23:41–100. https://doi.org/10.1016/S0927-796X(98)00009-6
40. Bordia RK, Kang S-JL, Olevsky EA (2017) Current understanding and future research directions at the onset of the next century of sintering science and technology. J Am Ceram Soc 100:2314–2352. https://doi.org/10.1111/jace.14919
41. Skorohod VV (1972) Rheological basis of the theory of sintering. Nauk Dumka, Kiev
42. Rahaman MN (2007) Sintering of Ceramics, CRC Press
43. German RM (1996) Sintering Theory and Practice, Wiley. Wiley
44. Manière C, Olevsky EA (2017) Porosity dependence of powder compaction constitutive parameters: Determination based on spark plasma sintering tests. Scr Mater 141:62–66. https://doi.org/10.1016/j.scriptamat.2017.07.026
45. Kraft T, Riedel H (2004) Numerical simulation of solid state sintering; model and application. J Eur Ceram Soc 24:345–361. https://doi.org/10.1016/S0955-2219(03)00222-X
46. Manière C, Harnois C, Marinel S (2021) 3D printing of porcelain and finite element simulation of sintering affected by final stage pore gas pressure. Mater Today Commun 26:102063. https://doi.org/10.1016/j.mtcomm.2021.102063

Figure captions

Figure 1 Bar deflection sintering test, a) configuration before sintering, b) lateral view of the sintered specimen.

Figure 2 Sintering anisotropy parametric analysis: a) effect of heating rate of 10 mm specimens, b) scale effect on specimens with diametric homothetic increase from 10 to 30 mm, c) filling ratio effect on 30 mm diameter samples, the filling architecture is shown on lower right by the yellow walls in the volume of the parts.

Figure 3 Sintering model identification from dilatometry tests, a) adjustment of the modeled specimen diameter and height, b) experimental and modeled porosity.

Figure 4 Modeling of the sintering deflection test by pore gas (a) and threshold (b) approaches, the creep based deflection magnitude has been modified via a parametric study on the shear viscosity terms.

Figure 5 a) Deflection curves for different shear viscosity factors, b) experimental vs optimum sintering simulation for the bar post-sintering deformation.

Figure 6 a) Optical microscopy of the sintering specimen microstructure, b) Al, Si elements EDSmap of the latter microstructure c) microstructure at the upper, middle, and lower part of a 10 mm diameter sintered specimen.

Figure 7 Mesoscale simulation of the layered microstructure assuming pore gas pressure and lower porosity in the layers interfaces, a) microstructural model structure, b) mesoscale simulated images of the shear deformations and effective sintering stress ($-P_l+P_{gas}$), c) simulated apparent shear viscosity vs continuum viscosity.

Figure 8 Mesoscale simulation of the layered microstructure assuming SiO_2 rigid inclusions, a) microstructural model structure, b) simulated apparent shear viscosity vs continuum viscosity for different content of SiO_2, c) mesoscale simulated images of the shear deformations.

Figure 9 a) Cup shape main reference dimensions, b,c) experimental radial corrective factor vs cup height to assumes the shape drying shrinkage on the initial simulated geometry for the small cup (b) and large cup (c).

Figure 10 Simulated small and large cup sintering with pore gas model (black lines correspond to the green shape dimensions) (a) and the threshold approach with shear viscosity correction (b).

Table captions

Table 2 Simulation/experiment dimensions comparison